Icarus 315 (2018) 115–123

Contents lists available at ScienceDirect

Icarus

journal homepage: www.elsevier.com/locate/icarus

The spatial distribution of Mercury's pyroclastic activity and the relation to lithospheric weaknesses

Christian Klimczak[a,*], Kelsey T. Crane[a], Mya A. Habermann[a,b], Paul K. Byrne[c]

[a] Structural Geology and Geomechanics Group, Department of Geology, University of Georgia, Athens, GA 30602, USA
[b] Institute of Meteoritics, Department of Earth and Planetary Sciences, University of New Mexico, Albuquerque, NM 87131, USA
[c] Planetary Research Group, Department of Marine, Earth, and Atmospheric Sciences, North Carolina State University, Raleigh, NC 27695, USA

ARTICLE INFO

Keywords:
Volcanism
Tectonics
Mercury

ABSTRACT

Mercury's surface preserves a rich history of volcanism, impact cratering, and tectonic deformation. Geological observations show that the earliest evidence of thrust faulting that was induced by the secular cooling and resulting global contraction of the planet coincided with the waning stages of effusive volcanism, but that explosive volcanism continued beyond this point. Stresses from global contraction, however, would have precluded efficient vertical magma ascent. Sites of pyroclastic activity—manifest as irregular depressions surrounded by diffuse, spectrally distinct halos—spatially coincide with lithospheric discontinuities, such as faults or those associated with impact craters. The vast majority of explosive vents are situated on the floors, rims, central peaks, or peak rings of impact structures. A substantial portion of such vents is also proximal to thrust faults: they are most spatially concentrated at or within 20 km of faults, with ever fewer vents progressively farther from tectonic structures. We statistically evaluated the spatial distribution of sites of pyroclastic activity with respect to faults and impact craters by generating sets of random point locations of equal count to those volcanic sites, computing their spatial relationship to the mapped faults and craters, and comparing them to our observations. We find that although the observed proximity of vents to faults is indistinguishable from a random distribution, their spatial association with impact craters is non-random. To examine the interrelatedness of several geospatial relationships of lithospheric weaknesses and pyroclastic activity, we performed a principal component analysis that tested correlations between vent size, the presence of vents within a crater, the diameters and degradation states of those craters, and vent distance from mapped faults, which help tie together interpretations of magma volumes and eruption energies, repeated utilization of magma pathways, and durations of eruptive events in the geological context of global contraction. Results reveal a predominance of small-sized vents indicative of short-lived, low-volume pyroclastic activity that are consistent with suppressed volcanism after the onset of global contraction. Greater size ranges of vents are found in large impact craters and when faults are nearby, which points to denser fracture networks facilitating magma ascent.

1. Introduction

Tectonism and volcanism on Mercury are closely intertwined, as both processes are tied to the thermal evolution of the planet. Its thermal history has largely been characterized by a long, sustained period of global contraction resulting from planetary cooling (Solomon, 1977). With the overall thermal state of the planet dominated by secular cooling, Mercury's continuously thickening lithosphere was subject to stresses from global contraction and so became increasingly inimicable to vertical magma ascent and widespread volcanic activity (Solomon, 1978; Wilson and Head, 2008). Instead, the contractional tectonic regime produced thrust faults (Solomon et al., 2008), manifest today as a global population of shortening landforms (Byrne et al., 2014; Figure 1) that began to form some 3–4 Ga ago (Banks et al., 2015; Crane and Klimczak, 2017). Geological observations and thermal evolution modeling together imply that widespread, dike-fed volcanism and major volcanic resurfacing were essentially limited to the time prior to global contraction (e.g., Solomon, 1978; Byrne et al., 2016).

However, geologic units interpreted as having been emplaced by explosive volcanism, on the basis of their spectral contrast with surrounding terrain, diffuse appearance, and spatial association with landforms thought to be volcanic vents (Head et al., 2009; Kerber et al., 2009), appear to have a broader range of ages (Goudge et al., 2014;

* Corresponding author.
E-mail address: klimczak@uga.edu (C. Klimczak).

https://doi.org/10.1016/j.icarus.2018.06.020
Received 5 April 2017; Received in revised form 16 June 2018; Accepted 19 June 2018
Available online 30 June 2018
0019-1035/

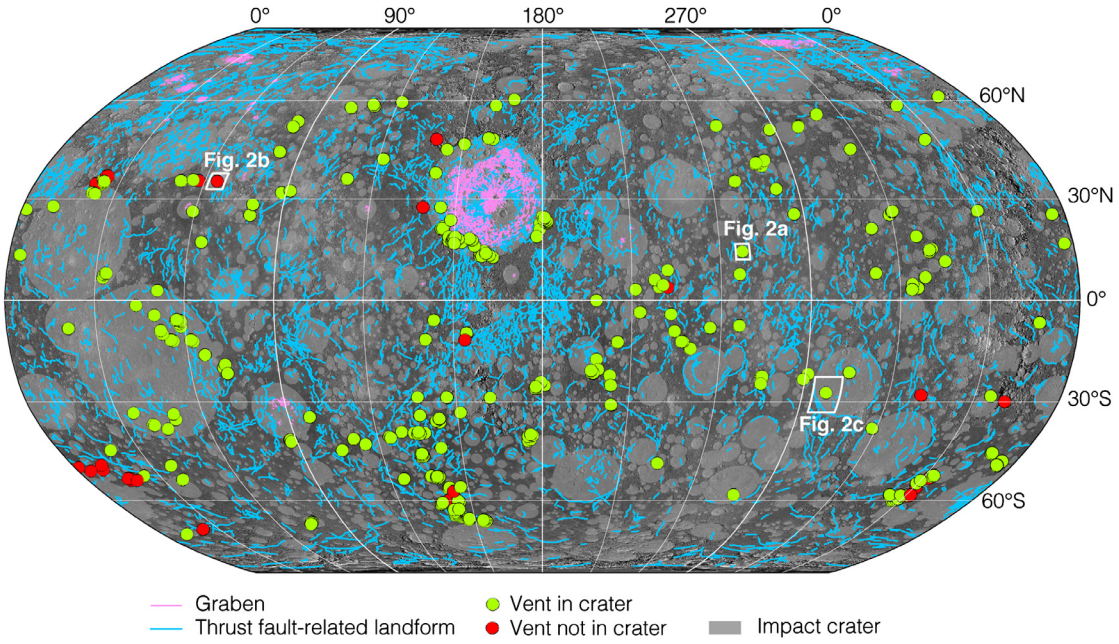

Fig. 1. The global distribution of vents associated with pyroclastic volcanism (dots), as well as normal- (pink lines) and thrust fault-related landforms (blue lines) shown on a global MESSENGER monochrome image mosaic in Robinson projection centered at 180°. Vents that occur in impact craters are in green; those that are not inside an impact crater are shown in red. Vent data after Thomas et al. (2015); fault data after Byrne et al. (2013, 2014). Impact craters (shown in light gray) after Fassett et al. (2011) and Kinczyk et al. (2016).

Thomas et al., 2014) that temporally overlapped with global contraction. Furthermore, many sites of pyroclastic activity occur within impact craters or along or near fault-related landforms (e.g., Goudge et al., 2014; Jozwiak et al., 2018).

Both fault-related landforms and impact craters represent lithospheric discontinuities. Faults are planar or zonal structures accommodating shear displacement via frictional sliding that include one or more slip planes (e.g., Schultz and Fossen, 2008), the fault core (a tabular zone of intense shear deformation: e.g., Childs et al., 1997), and a confining damage zone (e.g., Kim et al., 2004; Peacock et al., 2017). The largest faults on Mercury are found to reach depths of 35–40 km (e.g., Egea-Gonzáles et al., 2012). Impact craters create a damage zone beneath and surrounding the site of impact (e.g., Melosh, 1984; Ahrens and Rubin, 1993; Xia and Ahrens, 2001; Collins et al., 2004). In addition, complex craters and basins show abundant lithospheric-scale weaknesses with high degrees of deformation involving faulting and fracturing at the crater rim (e.g., Spray, 1997), crater floor (e.g., Kenkmann et al., 2013), and especially at central uplifts and peak ring structures (e.g., Morgan et al., 2000; Kenkmann et al., 2005; Osinski and Spray, 2005). The depth extent of impact crater damage zones is found to scale with a combination of factors, including impactor size, impact velocity, and target strength (e.g., Xia and Ahrens, 2001), so typically larger craters are expected to produce bigger and presumably deeper damage zones. The timescale and extent to which fractures on Mercury anneal through, for instance, formation of pseudotachylites or recrystallization in the lower crust remains largely unexplored. But crustal densities derived from Gravity Recovery and Interior Laboratory (GRAIL) measurements reveal that fractures introduced by impacts over the Moon's geologic past served to increase crustal porosities (e.g., Wieczorek et al., 2013), indicating that such fractures remain open and, thus, represent lithospheric weaknesses for a substantial amount of time.

In this study, we statistically evaluate if and how much impact craters and fault-related landforms and their associated lithospheric weaknesses are geospatially tied to sites of pyroclastic volcanism. Knowledge of how tectonic phenomena and pyroclastic volcanism interrelate has implications for the modes, locations, and timing of magma ascent on Mercury, especially for eruptions that occurred after the prevailing tectonic regime became dominated by global contraction.

2. Volcanic deposits and vents

Mercury's surface shows evidence for volcanic resurfacing, with plains interpreted to be volcanic in nature comprising almost a quarter of Mercury's surface (Denevi et al., 2013). These units are thought to have been emplaced as high-volume, short-duration flood basalts (Head et al., 2011; Byrne et al., 2013). The majority of such voluminous resurfacing ended at around the same time as the earliest evidence for thrust faulting is apparent (Byrne et al., 2016). Additionally, several hundred instances of pyroclastic deposits have been identified on Mercury, interpreted as such on the basis of their spectral contrast with surrounding terrain, diffuse appearance, geochemical signature, and spatial association with landforms regarded as volcanic vents (Kerber et al., 2009, 2011; Goudge et al., 2014; Thomas et al., 2015; Weider et al., 2016). The vents themselves are irregularly shaped depressions that lack the terraces and elevated rims that characterize impact craters.

The pyroclastic deposits show a broad geographic distribution (Kerber et al., 2011; Goudge et al., 2014; Thomas et al., 2015) (Fig. 1). Superposition relationships and crater size–frequency measurements indicate that the deposits collectively span a wide set of emplacement ages (Goudge et al., 2014; Thomas et al., 2014). Together, these observations indicate that pyroclastic activity on Mercury was much longer lived, although less voluminous, than effusive volcanism, and that explosive eruptions overlapped temporally with global contraction-induced thrust faulting (e.g., Banks et al., 2015; Crane and Klimczak, 2017). Furthermore, compound vents observed near the rim of the Caloris basin indicate that magma pathways may have been utilized repeatedly to produce multiple eruptions localized at these particular sites (Rothery et al., 2014). Volcanism, as a means of transporting material from depth to the surface, was therefore clearly not fully suppressed after the onset of global contraction.

We closely examined a number of pyroclastic units across Mercury

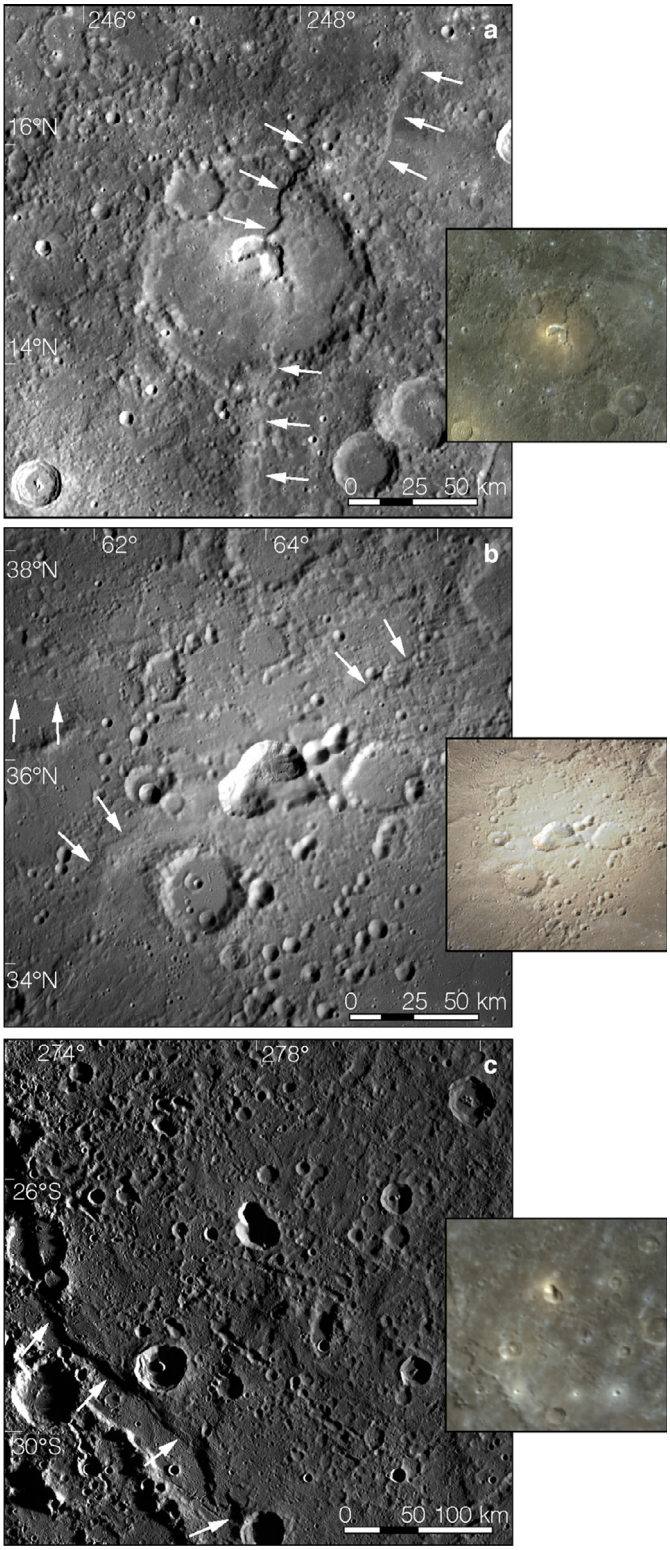

Fig. 2. The three study sites in this work. Each image of a pyroclastic deposit is in equirectangular projection, centered on the vent location and shown in monochrome (main figure) and in color (inset). (a) Site 1 features a pyroclastic deposit and vent in an impact structure (the Glinka crater) with nearby faults (marked by white arrows). The high-reflectance halo around the vent is the deposit itself. This halo appears as a red unit in the color mosaic with 1000 nm, 750 nm, and 430 nm narrow-band filters displayed in the red, green, and blue channels, respectively. (b) Site 2 includes three morphologically subtle expressions of thrust fault-related landforms (white arrows). The bright pyroclastic halo extends 150 km around the 40 km-diameter vent and has a pronounced multispectral difference with the surrounding units, as seen in the color mosaic. This pyroclastic deposit and vent is the biggest on Mercury. (c) Site 3 appears not to be spatially associated with a central peak or rim of an impact crater (although it is located on the floor of an inferred ancient impact basin). It is more than 150 km away from a thrust fault-related landform (white arrows). No bright halo is apparent in the monochrome mosaic, but a spectrally distinct region around the vent is found in the MESSENGER color mosaic. (For interpretation of the references to color in this figure legend, the reader is referred to the web version of this article.)

to identify a set of structural characteristics that may offer clues as to how explosive eruptions could persist after the start of this process. An exemplar site of pyroclastic volcanism, termed here “site 1”, is located in the center of the moderately-to-heavily degraded, ~90 km-diameter Glinka crater (Fig. 2a). Site 1 is characterized by a pronounced kidney-shaped depression that does not have a raised rim, which is surrounded by a bright halo visible in monochrome images but that stands out as a spectrally distinct unit in MESSENGER multispectral image mosaics (Fig. 2a). These observations are together consistent with interpretations of an explosive vent and its associated pyroclastic deposit (Kerber et al., 2011; Goudge et al., 2014). The vent has a surface area of ~200 km^2 (Thomas et al., 2015) and shows two long axes in map view oriented E–W and N–S, respectively. Three pronounced N–S-striking thrust fault-related landforms more than 50 km in length cut through the rim of Glinka, terminating at the vent (Fig. 2a).

A second volcanic site that we examine here (“site 2”) is a ~40 km-diameter kidney-shaped vent, surrounded by an ~150 km-wide pronounced bright halo (Fig. 2b) that forms a distinct unit in the multispectral image mosaic (Fig. 2). It is Mercury's best-studied explosive vent (Kerber et al., 2011; Thomas et al., 2014; Weider et al., 2016), and is the largest identified pyroclastic deposit on the planet (Weider et al., 2016). The vent itself has a surface area of ~900 km^2 (Thomas et al., 2015). The deposit spatially coincides with three < 30 km-long thrust fault-related landforms that have only subtle surface expressions in MESSENGER monochrome images. The thrust fault-related landforms are situated around 20 km distance to the vent. The long axis of the vent is oriented NE–SW, matching the strike of two of the proximal thrust fault-related landforms; the third structure strikes E–W (Fig. 2b). Site 2 does not occur within an impact crater, but several impact craters of various degradation stages and diameters of up to ~25 km are nearby.

An additional site of pyroclastic volcanism (Thomas et al., 2015)—that we term here “site 3”—is situated on the floor of an ancient, degraded, heavily modified, ~885 km-diameter basin (Fassett et al., 2012; Kinczyk et al., 2016), but is not associated spatially with that basin's rim or central peak structure. The vent at site 3 is a 35 km wide irregular depression that lacks a bright halo in monochrome images but shows a spectrally distinct unit only directly on and next to the vent (Fig. 2). The vent has a surface area of 700 km^2 (Thomas et al., 2015). Approximately 150 km to the southwest is a prominent, ~400 km-long thrust fault-related landform (Fig. 2c). This tectonic structure strikes NW–SE, closely matching the orientation of the long axis of the vent.

On the basis of their spatial association with structural discontinuities, these three sites are representative of > 91% of all explosive volcanic deposits on Mercury, as they occur either within impact craters or basins, within < 20 km of faults, or both (Fig. 1). We find that only 29 of 327 previously surveyed vents on Mercury (Thomas et al., 2015) do not occur within impact craters or in proximity to faults. Our examination of these three sites indicates that vent size and shape, distance to faults, size of the nearest fault, location within an impact structure, and size and degradation stage of impact structure play controlling roles in the manifestation of pyroclastic activity on Mercury.

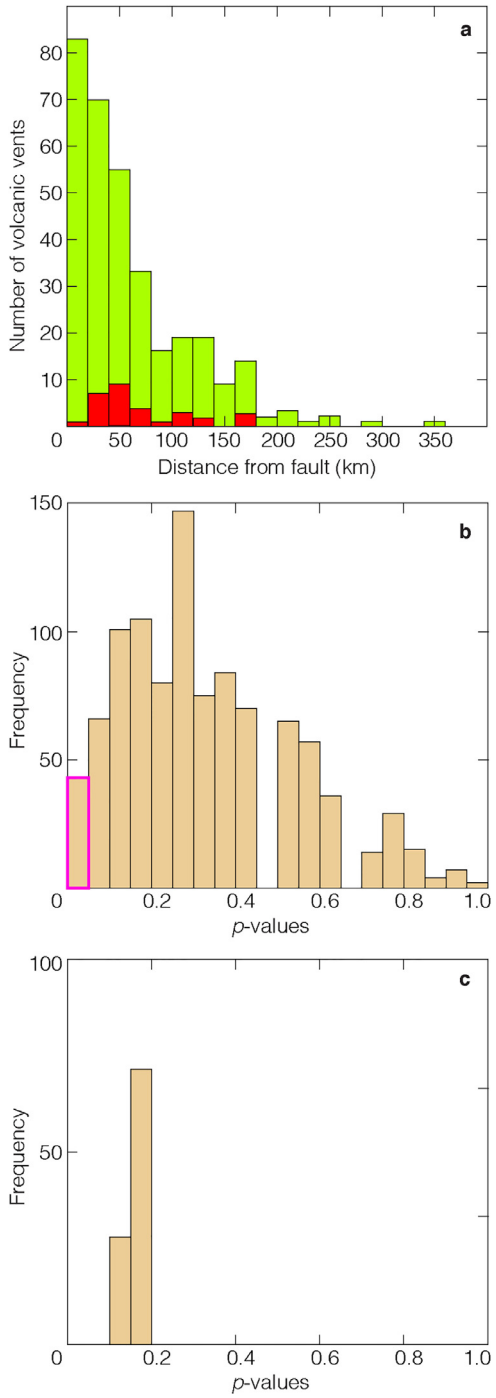

Fig. 3. Histograms illustrating the distance of pyroclastic vents from the closest thrust fault-related landforms. (a) The observed distances of 327 volcanic vents from the nearest fault, in bins of 20 km; vents inside impact craters are green, and those outside craters are red. (b) A histogram showing the number of *p*-values from the Kolmogorov–Smirnov statistic for 1000 numerical runs of the distance from faults (brown bins) for 327 randomly computed points on Mercury. Only 43 runs of random distributions (the bin outlined in magenta) are significantly different (with 95% confidence); the remaining 957 runs produce vent–fault distances that are statistically indistinguishable from the observed distribution shown in (a). (c) A histogram of *p*-values computed from *z*-tests for 100 numerical runs for the proportions of 327 random point on Mercury located in the observed population of impact craters. (For interpretation of the references to color in the text, the reader is referred to the web version of this article.)

3. Pyroclastic units occur at or near lithospheric weaknesses

Numerous pyroclastic deposits and their vents have previously been reported as being collocated with the floors, central peaks, or rims of impact structures, or with thrust fault-related landforms (e.g., Goudge et al., 2014), suggesting that weaknesses in Mercury's lithosphere played a role in the ascent and eruption of magmas after the onset of global contraction. To investigate this prospective influence, we conducted a geospatial analysis to quantify the locations of explosive volcanic sites with respect to impact structures using as inputs craters identified by Fassett et al. (2011, 2012) and Kinczyk et al. (2016), and fault-related landforms using mapping observations by Byrne et al. (2013, 2014).

Our results reveal that the vast majority of vents occur within impact craters and/or near normal and thrust fault-related landforms (Fig. 1). Of 327 sites, 297 (~91% of this total) are situated on the floors, rims, central peaks, or peak rings of craters (with those craters being larger in size than the vent). In contrast, only 30 (~9%) explosive volcanic sites are *not* situated on the floors, rims, central peaks, or peak rings of craters. This analysis shows that pyroclastic activity on Mercury is predominantly found within impact structures.

We also quantified vent locations in terms of distance from a fault, as measured by nearest distance of fault to the center of the mapped vent. Explosive vents are most spatially concentrated at or within 20 km of a fault (n = 82), and their numbers drop off progressively farther away from tectonic structures (Fig. 3a). This relationship implies that pyroclastic activity is more likely than not to be spatially collocated with faulting.

4. Statistical evaluation of vent locations and lithospheric discontinuities

4.1. Vents and faults

We next tested whether the correlation of the spatial distribution of pyroclastic sites with faults is statistically significant, or whether the great number of widely distributed faults on Mercury (Fig. 1) may simply cause any random population of 327 points to produce a similar distribution. To do so, we generated 1000 sets of 327 random points on the surface of Mercury and quantified their shortest horizontal (geodesic) distances from faults. We compared the distributions of distances to the nearest fault for our 1000 randomly located populations of 327 points with the corresponding distances between vents and their nearest fault (computed from earlier studies (Byrne et al., 2013, 2014)) with a Kolmogorov–Smirnov statistical test and its associated *p*-value (Fig. 3b). The *p*-value is a measure of similarity between the compared distributions with values ranging from 0 to 1, where 0 indicates no similarities and 1 indicates identical distributions. Of our 1000 randomly generated distributions, only 43 have *p*-values below 0.05 and so are significantly different at the 95% confidence level from the observed distribution shown in Fig. 3a (Fig. 3b, bin with magenta outline). The overwhelming majority of simulated random distributions show *p*-values larger than 0.05 and so are statistically indistinguishable at the 95% confidence level from the observed distribution of vent distance from faults (Fig. 3b).

This result could imply that the observed proximity to faults for a large number of pyroclastic vents on Mercury is random and that, in turn, magma ascent may not be facilitated along faults or along fractures within fault damage zones any more readily than for areas where faults are not present. Nonetheless, thrust faulting on Mercury is so pervasive that a prospective control over pyroclastic eruptive activity cannot be unequivocally discounted.

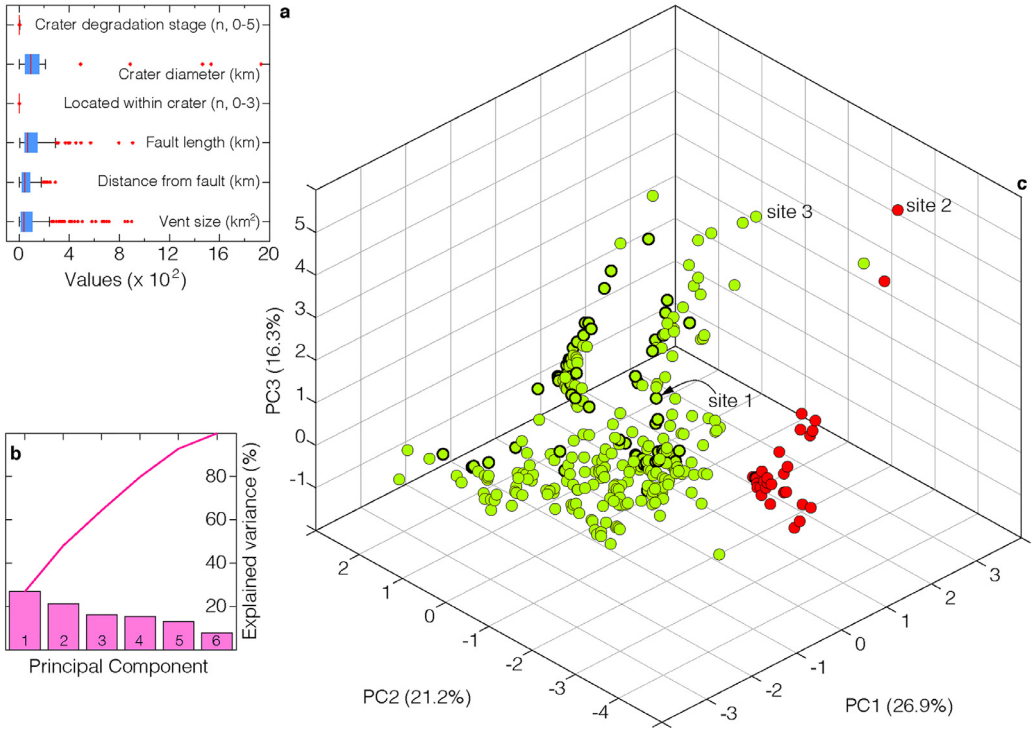

Fig. 4. Results of our weighted principal component analysis. (a) Box-and-whisker plots showing the variability of the investigated parameters. (b) Scree plot highlighting the contribution of variability of data for each principal component; together, the first three principal components account for approximately two thirds of the data variability. (c) Centered and scaled observations of vents projected onto the first three principal components, highlighting a clustering of the different categories of vents. (Vent symbology is as for Fig. 1).

4.2. Vents and impact craters

The possibility that there is a sufficient density of suitably oriented lithospheric weaknesses within Mercury's lithosphere caused by impacts for magmas to utilize for ascent is supported by the number of vents (~91%) that occur within large (>20 km) impact craters. In turn, the percentage of Mercury's surface covered by preserved impact craters (Fassett et al., 2011, 2012) is only 43%. That ~91% of a population of randomly located vents fall within only 43% of the total area of Mercury seems very unlikely, and thus we statistically evaluated whether the locations of pyroclastic sites are in fact dependent upon impact craters. We simulated 100 sets of 327 randomly distributed points on the surface of Mercury, and then counted the points and proportion of points inside impact craters for each set. The resulting proportions of random points present in impact craters ranged from 35% to 47%, with an average of 42%, a number very similar to the proportion of Mercury's surface covered by impact craters.

To better quantify if the observed vent distribution could be distinguished from our 100 randomly generated distributions, we performed *z*-tests that compared each simulated proportion to the observation. The result of each test was interpreted again in terms of a *p*-value, which allowed us to evaluate the significance of the difference between the observed and simulated proportions. All *p*-values for this analysis fall between 0.1 and 0.2 (Fig. 3c), indicating that if vents were indeed randomly distributed with respect to impact craters, the probability of observing a population with a similar distribution to our observed population would be less than 20%. When a *z*-test was performed across all 100 simulations, the collective *p*-value dropped to less than 1×10^{-5}. This very low value indicates that there is a statistically significant difference between the observed proportion of vents inside impact craters and that expected from a random distribution of 327 locations. This result in turn implies that, with over 99% confidence, it is very likely that the observed distribution of pyroclastic vents on Mercury is controlled by pre-existing impact structures and their associated lithospheric weaknesses.

4.3. Vents, faults, and impact craters

We also conducted a principal component analysis (PCA) to gain a deeper understanding of the relationship between pyroclastic deposits and lithospheric weaknesses. Based on our observations (Section 2) and geospatial calculations (Section 3), we extracted geospatial relationships of lithospheric weaknesses and pyroclastic activity for each of the 327 vents. In particular, we compiled vent size (as defined by the area enclosed by the outline of the pit); distance between vent center and mapped faults (Fig. 3a); the length of the fault nearest to a vent; and whether a vent is located within one or several superposing impact structures and, if so, the diameter and degradation state of the crater(s). The list of values for these parameters and the results of the PCA are provided as supplementary material.

The within-group variation of our investigated variables is displayed in the box-and-whisker plot in Fig. 4a. The red vertical lines for each variable represent their median values, thus dividing each set of variables into two halves. The upper and lower boundaries of the blue boxes represent the medians of the upper (75th percentile) and lower halves (25th percentile) of the group, and indicate the likely range of variation of the variables. The whiskers show the range between the highest and lowest values that are not considered outliers. Outliers (red dots) are defined by values exceeding or falling below 2.7 times the standard deviation of each group.

The within-group variation of each of our investigated variables is unequal and shows considerable differences in range (Fig. 4a), in part because some of the variables are classified as ordinal or interval data whereas others are ratio data, and because the scales of measurement within length- and size-related variables are different. For example, the values for vent distance from fault, as well as vent size, fault length, and impact crater diameters, range over two or three orders of magnitude. Most observations within these categories occur on the lower end, with several outliers on the upper end of the scale (Fig. 4a), and the distributions are all skewed right with outliers of up to two orders of magnitude larger than the median. In contrast, there is little variation in

Table 1
Coefficients of the first three principal components of the weighted principal component analysis. Coefficients with magnitudes greater than 0.5 are bolded.

Variable	PC1	PC2	PC3
Vent size	0.26	–0.14	**0.88**
Distance from fault	–0.27	**–0.55**	0.07
Fault length	–0.16	–0.43	0.25
Located within crater	**–0.58**	0.34	0.23
Crater diameter	0.28	**0.57**	0.26
Crater degradation stage	**–0.64**	0.22	0.18

the range of values for vents located in impact craters (a value representing the number of craters associated with the vent from $n = 0$ to a maximum of $n = 3$) and for crater degradation states (which includes a classification of 0 for vents not located in impact craters, and categories 1–5 per a convention for characterizing such states (cf. Kinczyk et al., 2016)).

A PCA transforms a set of observations of potentially correlated variables into independent new variables, which are linear combinations of those original variables. An understanding of these new variables requires an interpretation of the combinations of old variables with respect to the environmental, spatial, or geological context of our investigated problem. The new axes, or principal components, represent directions of large variation within the data. The difference in units, and the large range, of our variables (Fig. 4a) require a weighted PCA, for which we took as weights the inverse variances of our variables. Inverse-variance weighting is typically used in statistics to combine the results from independent measurements. The PCA returns the variance explained by each principal component, the coordinates of the original data in the new coordinate system to which all variables contribute (i.e., component scores), and the coefficients of the principal components that indicate the contribution of each variable toward a given principal component.

The percentages of explained variance for each of the principal components are shown in the scree plot for our PCA (Fig. 4b). This figure highlights the relative contribution of the individual principal components to the overall variability of the data. The first three principal components of our analysis account for approximately two thirds of the variability of data, but principal components 4 through 6 explain less than their share of the variation, under the assumption that variation is equal across all components (i.e., that each component is responsible for 16% of the total variation). The component scores and coefficients of the first three principal components may thus be used to interpret our data.

The coefficients of the first three principal components represent a combination of variables: higher absolute values of coefficients for a particular variable indicate greater influence on the principal component (the bolded coefficients in Table 1). The first principal component (PC1), which accounts for ~27% of the variability of our data, is most influenced by both the location of a vent within one or more impact craters and by the degradation state of the crater(s) in which it is located (Table 1). The second principal component (PC2), which accounts for ~21% of the data variability, is governed by the diameter of the impact crater in which the vents are located and the distance of vents from faults (Table 1). The third principal component (PC3) is dominated by vent size (Table 1), and accounts for ~16% of the data variability.

The individual component scores of the PCA highlight the dependence of the principal components on one another (Fig. 4c). The largest component scores in PC1 correspond to vents that are not inside an impact crater (red dots), and large component scores for vents inside impact craters (green dots) indicate that they are present in more heavily degraded impact craters. Lower first principal component scores correlate with vents inside fresher impact craters. Large component scores in PC2 represent vents in large impact craters and/or close to a fault (boldly outlined dots indicate vents within 20 km of a fault), and lower component scores correspond to vents in smaller impact craters or those not located within an impact crater or near a fault. Larger component scores in PC3 represent vents with a larger surface area.

Our findings show that there is a trend between the component scores of PC1 and PC3 (Fig. 4), which points to a tendency for vents to be larger in more heavily degraded impact craters and for them to be smaller in fresh impact craters. For vents inside impact craters (green dots), larger scores in PC2 generally correspond to larger scores in PC3, which shows that there may also be a dependence on vent size of impact crater diameter and/or distance to a fault. We therefore further compared the ranges of several vent size sub-populations with one another (Fig. 5). The sub-populations were derived based on the dominant variables of our first two principal components.

The vent size variation for different sub-populations is again displayed as a box-and-whisker plot (Fig. 5). As with Fig. 4a, the red (now horizontal) lines for each variable represent the median, the boxes indicate the likely range of variation (75th and 25th percentile of the group), and the whiskers show the range between the highest and lowest values that are not considered outliers (i.e., those values beyond 2.7 σ of each group). Due to the difference in sub-population sizes of vent sizes, we display our confidence in the sub-population statistics in levels of transparency computed from their individual margins of error adjusted for finite population sizes (Fig. 5, blue values). The margin of error is a common statistic used to express confidence in data trends. The sub-populations of vent sizes are shown in comparison to the total range of vent sizes (N, Fig. 5a). The clustering of the different categories of vents as a function of their first three principal components, the observed trends in the scatter of the scores (Fig. 4c), as well as the vent size population statistics (Fig. 5), allow us to interpret and discuss several relationships between combinations of these variables that might not otherwise have been obvious.

5. Discussion

Our principal component analysis reveals that PC1 is most influenced by both the location of a vent within one or more impact craters and by the degradation state of the impact crater(s) in which it is located (Table 1). Impact cratering is a stochastic process (e.g., Le Feuvre and Wieczorek, 2011), such that the superposition relationships of two or even three craters are more likely to have occurred over longer time intervals, and the morphological degradation of impact craters is also primarily a function of time (Spudis and Guest, 1988). We thus interpret PC1 to represent the variability of our 327 data points with respect to time.

We show that PC2 is governed by both the diameter of the impact crater in which the vents are located, and the distance of vents from faults (Table 1). Larger impact craters are accompanied by larger impact damage zones (e.g., Xia and Ahrens, 2001), and similarly, the density and size of fractures within the fault damage zone increases with increasing proximity of the zone of most intense shear deformation (e.g., Kim et al., 2004; Faulkner et al., 2011). We therefore interpret PC2 to represent the variability of our data with respect to the density and interconnectedness of fractures and fracture networks in Mercury's lithosphere. That the distance between vents and faults accounts for much of the variability of the data further supports our interpretation that thrust faulting on Mercury is so pervasive that sites of pyroclastic activity tend to be located near faults merely because of happenstance.

PC3 is dominated by vent size (Table 1). The dimensions of a pyroclastic vent are in part a function of size and energy of the eruption, which in turn can reflect the volume of magma and volatiles erupted there (e.g., Kerber et al., 2009; Weider et al., 2016). Additionally, repeated utilization of magma pathways to produce compound vents (Rothery et al., 2014) may have also served to increase the cumulative size of the vent(s). Therefore, PC3 is interpreted to represent the

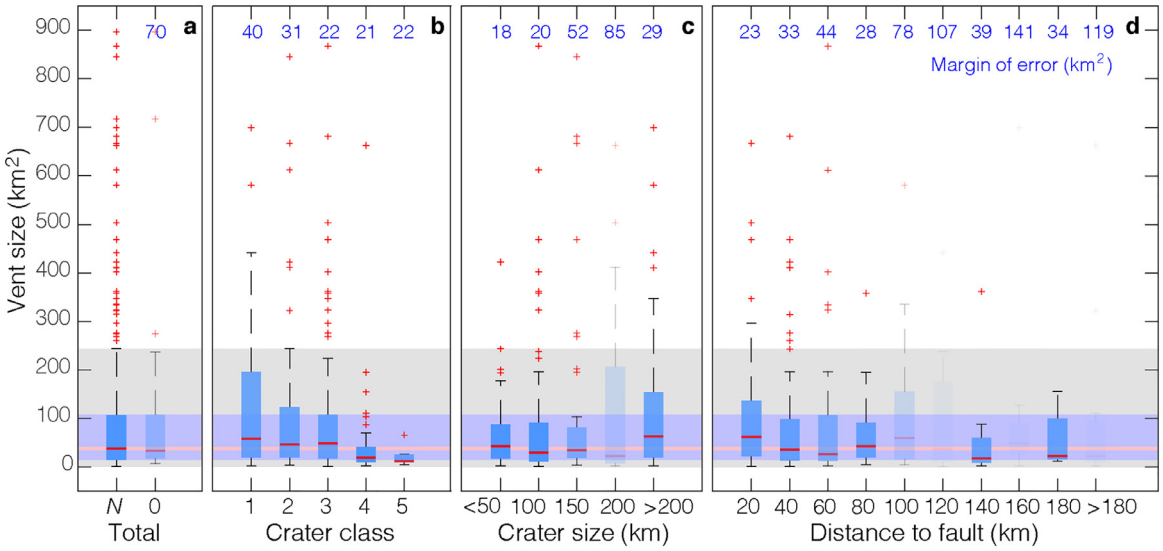

Fig. 5. Box-and-whisker plots of vent sizes calculated for various sub-populations of vents. Different transparencies of sub-populations of vents in impact craters are reflective of the margin of error (blue numbers in top row), which was taken as a measure of confidence in the sub-population vent size range. The red, blue, and gray shadings throughout all parts of the figure are representative of the median, likely range of values, and the highest and lowest values for the total population of vents, respectively. (a) Size ranges of the total population of vents (*N*) and all vents outside of craters (0). (b) Size ranges of vents within craters grouped by degradation class (i.e., 1 = most degraded, 5 = least degraded) of the crater. Vents tend to be bigger in more degraded (and thus presumably older) craters. (c) Size ranges of vents within craters grouped by crater size. Smaller craters tend to host vents with generally smaller size ranges, whereas bigger impact structures tend to host vents that show larger size ranges. (d) Size ranges of vents within craters arranged by their distance from a fault. Small vents occur at any distance to faults, but larger vents tend to be closer to faults. (For interpretation of the references to color in this figure legend, the reader is referred to the web version of this article.)

variability of our data with respect to a combination of erupted magma volume (and volatile content) and duration and/or complexity of volcanic activity at the vent location. (Mass wasting is also likely to modify vent shape and size, but not to the extent of eruption volume and repetition.)

Given these interpretations, the relationships among the first three principal components (Fig. 4c) points to a complex interrelatedness between time, the density and connectivity of fractures in the lithosphere, and magma volume, volatile content, and duration of explosive activity on Mercury. The relationships between vent size and impact crater degradation, as well as between vent size and impact crater diameter and/or distance to faults, may thus be explored further:

Most vents are small. Vents with small surface areas have low scores in PC3 and most vents show low PC3 scores (Fig. 4c). Moreover, small vents are the most numerous across all analyzed sub-populations of vent sizes, as evinced by all sub-population medians being skewed toward smaller vent surface areas (Fig. 5). An abundance of small vent sizes across the planet, and across all analyzed vent sub-populations, indicates that the preserved record of pyroclastic activity on Mercury was generally limited by either small magma volumes or eruption energies (and volatile content), utilization of pathways of magmas in a single or in a limited number of eruptions, short-duration eruptions, or a combination of all of these factors.

This predominance of small-sized vents and its implications are consistent with suppressed volcanism and vertical magma ascent after the onset of global contraction (e.g., Solomon, 1978; Wilson and Head, 2008). However, this finding also highlights the importance of larger vents for understanding magma ascent and volcanic eruptions in contractional tectonic regimes. Larger pyroclastic vents likely saw some combination of increased magma volumes and eruption energies, repeated utilization of magma pathways, and a prolonged duration of individual eruptions. A primary example is site 2, which features the largest recognized vent and associated pyroclastic deposit on Mercury (Fig. 2b). The size of the vent and its encircling deposit indicate that the eruption energy was likely larger than for most other deposits on Mercury and/or that magmas utilized pathways for a longer time than other sites of pyroclastic volcanism.

Vents are larger in more heavily degraded and thus presumably older impact craters, and are smaller in morphologically fresh and thus presumably younger impact craters. Vents in more heavily degraded impact craters have positive scores in PC1, whereas vents in morphologically fresh craters have negative PC1 scores; larger vents also have larger scores in PC3 (Fig. 4c). Furthermore, vents in craters show a clear trend in their size ranges when host craters are subdivided into different crater degradation classes. In particular, class 1 craters (representing the most heavily degraded and presumably oldest craters: Spudis and Guest, 1988) host vents with the largest range in vent surface area, including some of the largest vents (Fig. 5b). The range in vent size decreases with increasing crater class—with class 5 craters (the least degraded and presumably youngest craters) hosting the smallest vents (Fig. 5b).

Impact damage zones likely contain many thousands of fractures, with the greatest deformation at impact crater rims, central peaks, and peak ring structures (e.g., Kenkmann et al., 2013). Central peaks and peak rings, in particular, are heavily faulted, fractured, and brecciated (Morgan et al., 2000, 2016; Kenkmann et al., 2005; Osinski and Spray, 2005) and originate from a minimum of a few to a few tens of kilometers depth (Ernst et al., 2010). Under the assumption that annealing of fractures does not play a major role, those fractures associated with older impact craters are present within the lithosphere for a longer period of time and thus have a greater chance to be utilized (repeatedly) by magmas as pathways to the surface.

The time component thus plays a dominant role for a greater number of vents to be larger inside older impact craters. However, this correlation does not tell us whether the eruptive activity itself is old, as explosive volcanism may have taken place any time after the emplacement of the impact crater (perhaps even repeatedly: Rothery et al., 2014). Younger impact craters (per their degradation state) that host pyroclastic units, on the other hand, tend also to host smaller vents. This correlation implies that volcanism within these impact craters is not only correspondingly young, and that the time window for these magmas to utilize fractures associated with these craters was relatively short, but magma volumes and thus the release of volatiles during the explosive eruptions was comparatively low in the geologically recent.

That heavily degraded impact craters also host many small vents may be reflective of short-lived, low-volume pyroclastic activity at these sites as well.

The size range of vents tends to be greater in large impact craters and when a fault is nearby. Vents in large impact craters that are near faults have high scores in PC2 and in PC3 (Fig. 4c). Furthermore, the size ranges in craters between 150 and 200 km (with low confidence), and in craters above 200 km in diameter (with high confidence), are greater than those for craters with smaller diameters (Fig. 5c). Additionally, we find with high confidence that the vent size range is greatest for vents in craters within 20 km of a fault, with the highest median values across all sub-populations (Fig. 5d). Large vents also occur away from faults (Fig. 5d), such as the vent at site 3, but there is a low number of vents in these particular sub-populations that reduces the confidence in the size ranges.

The penetration depth, spatial density, and interconnectedness of fractures in impact damage zones is likely greater for large impact craters than small ones. The proximity to faults is also accompanied by an increase in fracture spatial density and interconnectedness as part of the fault damage zone. Larger impacts were more common earlier in the geological history of Mercury and so they tend to be older. Therefore it is no surprise that larger vents are also correlated with more heavily degraded impact craters (see our second point, above). In addition, the probability of faults developing within or near older and larger craters is greater (Crane and Klimczak, 2017). Thus there were higher chances, spatially and temporally, for fault damage zones to interact with impact crater damage zones and form denser and more interconnected fracture networks than would otherwise be possible for faults or impact craters separately. Such fracture networks would be present for a considerable amount of time and would possess the greatest number of discrete structures with suitable orientations and conductivities for facilitating the (repeated) ascent of magma.

As shown in Section 4.1, the result of our simulations to test the spatial distribution of vents with respect to faults could indicate that the observed proximity to faults for a large number of pyroclastic vents is random and that, in turn, magma ascent along pre-existing faults or within fault damage zones may not be common on Mercury. However, this finding does not necessarily preclude some control of magma migration through Mercury's lithosphere under the influence of slip events on faults. That a large portion of pyroclastic activity, including a greater amount of large volcanic vents (Figs. 4c, 5d), is observed within 20 km of faults (Fig. 3a) indicates that faulting must be pervasive throughout Mercury's lithosphere. Additional testing is required to discriminate whether the increased vent size range associated with pyroclastic activity in large impact craters, and within 20 km of faults, can be distinguished from random. Nonetheless, we hypothesize that slip events on thrust faults and their associated stress changes (e.g., King et al., 1994) may alter the regional stresses from global contraction. This alteration may serve to unload suitably oriented pre-existing fractures in impact crater damage zones, thus allowing for magma ascent and the increase in vent size by repeated or prolonged eruption.

6. Conclusions

Statistical simulations and analyses were used in this study to obtain insight into the spatial distribution of pyroclastic volcanism, and its relation to lithospheric weaknesses, on Mercury. Observations indicate that pyroclastic activity most often occurred near fault-related landforms (Fig. 3a) and within impact craters and basins (Fig. 1). Our statistical simulations reveal, however, that the relationship between faults and sites of pyroclastic activity cannot be distinguished from random. We attribute this finding to pervasive faulting on Mercury, such that pyroclastic volcanism has a tendency to be located near faults purely through circumstance and without the need for magma to utilize faults or other fractures within fault damage zones.

Our statistical simulations further indicate that the spatial relationship of impact craters and sites of pyroclastic activity can be distinguished from random. We further investigated this finding by means of principal component analysis. Based on our observations of different sites of pyroclastic activity, we focused this analysis on the size of the pyroclastic eruption, the location within an impact structure, the size and degradation stage of the impact structure, and the distance to and length of the nearest fault. The results of the principal component analysis are consistent with photogeological observations: that there is a strong spatial and likely temporal link between pyroclastic volcanism and pre-existing lithospheric weaknesses associated with impact craters. Most pyroclastic vents on Mercury are small (compared with the size range of vents on Mercury), the range of vent sizes is greater in more heavily degraded and thus presumably older craters, and the size range of vents tends to be greater in large craters and when a fault is nearby.

These findings effectively place constraints on magma volumes and eruption energies and repeated utilization of magma pathways of individual eruptions in the geological context of global contraction. Our result that most pyroclastic vents on Mercury are small is consistent with the view that volcanism was tempered by the onset of global contraction. Equally, we demonstrate the importance of larger vents, and their spatial relationship to lithospheric weaknesses, for understanding magma ascent and volcanic eruptions in contractional tectonic regimes in general, as those larger vents occur in areas we interpret to be more densely fractured.

Acknowledgments

We thank Caleb I. Fassett and Mallory J. Kinczyk for providing and discussing the crater datasets for Mercury. We thank Eric H. Christiansen, Rónadh Cox, and Robert Anderson, as well as an anonymous referee, for their helpful comments during the review of this paper. CK acknowledges support from University of Georgia faculty start-up funds. PKB acknowledges support from North Carolina State University faculty start-up funds.

Supplementary materials

Supplementary material associated with this article can be found, in the online version, at doi:10.1016/j.icarus.2018.06.020.

References

Ahrens, T.J., Rubin, A.M., 1993. Impact-induced tensional failure in rock. J. Geophys. Res. 98 (E1), 1185–1203. http://dx.doi.org/10.1029/92JE02679.

Banks, M.E., Xiao, Z., Watters, T.R., Strom, R.G., Braden, S.E., Chapman, C.R., Solomon, S.C., Klimczak, C., Byrne, P.K., 2015. Duration of activity on lobate-scarp thrust faults on Mercury. J. Geophys. Res. Planets 120, 1751–1762. http://dx.doi.org/10.1002/2015JE004828.

Byrne, P.K., Klimczak, C., Blair, D.M., Ferrari, S., Solomon, S.C., Freed, A.M., Watters, T.R., Murchie, S.L., 2013. Tectonic complexity within volcanically infilled craters and basins on Mercury. Lunar Planet. Sci. 44 abstract 1261, Houston, Texas.

Byrne, P.K., Klimczak, C., Şengör, C.A.M., Solomon, S.C., Watters, T.R., Hauck II, S.A., 2014. Mercury's global contraction much greater than earlier estimates. Nat. Geosci. 7 (4), 301–307. http://dx.doi.org/10.1038/ngeo2097.

Byrne, P.K., Ostrach, L.R., Fassett, C.I., Chapman, C.R., Denevi, B.W., Evans, A.J, Klimczak, C., Banks, M., Head, J.W., Solomon, S.C., 2016. Widespread effusive volcanism on Mercury likely ended by about 3.5 Ga. Geophys. Res. Lett. 43, 7408–7416. http://dx.doi.org/10.1002/2016GL069412.

Childs, C., Walsh, J.J., Watterson, J., 1997. Complexity in fault zone structure and implications for fault seal prediction. In: Møller-Pedersen, P, Koestler, A.G. (Eds.), Hydrocarbon seals: Importance for Exploration and Production. Norwegian Petroleum Society, Special Publication 7 (Elsevier), Singapore, pp. 61–72.

Collins, G.S., Melosh, H.J., Ivanov, B.A., 2004. Modeling damage and deformation in impact simulations. Meteorit. Planet. Sci. 39 (2), 217–231. http://dx.doi.org/10.1111/j.1945-5100.2004.tb00337.x.

Crane, K.T., Klimczak, C., 2017. Timing and Rate of Global Contraction on Mercury. Geophys. Res. Lett 44, 3082–3089. http://dx.doi.org/10.1002/2017GL072711.

Denevi, B.W., Ernst, C.M., Meyer, H.M., Robinson, M.S., Murchie, S.L., Whitten, J.L., Head, J.W., Watters, T.R., Solomon, S.C., Ostrach, L.R., Chapman, C.R., Byrne, P.K., Klimczak, C., Peplowski, P.N., 2013. The distribution and origin of smooth plains on Mercury. J. Geophys. Res. 118 (5), 891–907. http://dx.doi.org/10.1002/jgre.20075.

Egea-González, I., Ruiz, J., Fernández, C., Williams, J.-P., Márquez, Á., Lara, L.M., 2012. Depth of faulting and ancient heat flows in the Kuiper region of Mercury from lobate scarp topography. Planet. Space Sci. 60, 193–198.

Ernst, C.M., Murchie, S.L., Barnouin, O.S., Robinson, M.S., Denevi, B.W., Blewett, D.T., Head, J.W., Izenberg, N.R., Solomon, S.C., Roberts, J.H., 2010. Exposure of spectrally distinct material by impact craters on Mercury: Implications for Global Stratigraphy. Icarus 209, 210–223. http://dx.doi.org/10.1016/j.icarus.2010.05.022.

Fassett, C.I., Kadish, S.J., Head, J.W., Solomon, S.C., Strom, R.G., 2011. The global population of large craters on Mercury and comparison with the Moon. Geophys. Res. Lett. 38, L10202. http://dx.doi.org/10.1029/2011GL047294.

Fassett, C.I., Head, J.W., Baker, D.M.H., Zuber, M.T., Smith, D.E., Neumann, G.A., Solomon, S.C., Klimczak, C., Strom, R.G., Chapman, C.R., Prockter, L.M., Phillips, R.J., Oberst, J., Preusker, F., 2012. Large impact basins on Mercury: global distribution, characteristics, and modification history from MESSENGER orbital data. J. Geophys. Res. 117, E00L08. http://dx.doi.org/10.1029/2012JE004154.

Faulkner, D.R., Mitchell, T.M., Jensen, E., Cembrano, J., 2011. Scaling of fault damage zones with displacement and the implications for fault growth processes. J. Geophys. Res. 116, B05403. http://dx.doi.org/10.1029/2010JB007788.

Goudge, T.A., Head, J.W., Kerber, L., Blewett, D.T., Denevi, B.W., Domingue, D.L., Gillis-Davis, J.J., Gwinner, K., Helbert, J., Holsclaw, G.M., Izenberg, N.R., Klima, R.L., McClintock, W.E., Murchie, S.L., Neumann, G.A., Smith, D.E., Strom, R.G., Xiao, Z., Zuber, M.T., Solomon, S.C., 2014. Global inventory and characterization of pyroclastic deposits on Mercury: new insights into pyroclastic activity from MESSENGER orbital data. J. Geophys. Res. 119, 635–658. http://dx.doi.org/10.1002/2013JE004480.

Head, J.W., Murchie, S.L., Prockter, L.M., Solomon, S.C., Strom, R.G., Chapman, C.R., Watters, T.R., Blewett, D.T., Gillis-Davis, J.J., Fassett, C.I., Dickson, J.L., Hurwitz, D.M., Ostrach, L.R., 2009. Evidence for intrusive activity on Mercury from the first MESSENGER flyby. Earth Planet. Sci. Lett. 285, 251–262,. http://dx.doi.org/10.1016/j.epsl.2009.03.008.

Head, J.W., Chapman, C.R., Strom, R.G., Fassett, C.I., Denevi, B.W., Blewett, D.T., Ernst, C.M., Watters, T.R., Solomon, S.C., Murchie, S.L., Prockter, L.M., Chabot, N.L., Gillis-Davis, J.J., Whitten, J.L., Goudge, T.A., Baker, D.M.H., Hurwitz, D.M., Ostrach, L.R., Xiao, Z., Merline, W.J., Kerber, L., Dickson, J.L., Oberst, J., Byrne, P.K., Klimczak, C., Nittler, L.R., 2011. Flood volcanism in the northern high latitudes of Mercury revealed by MESSENGER. Science 333, 1853–1856. http://dx.doi.org/10.1126/science.1211997.

Jozwiak, L.M., Head, J.W., Wilson, L., 2018. Explosive volcanism on Mercury: Analysis of vent and deposit morphology and modes of eruption. Icarus 302, 191–212. http://dx.doi.org/10.1016/j.icarus.2017.11.011.

Kenkmann, T., Jahn, A., Scherler, D., Ivanov, B.A., 2005. Structure and formation of a central uplift: a case study at the Upheaval Dome impact crater, Utah. In: Kenkmann, T, Hörz, F, Deutsch, A (Eds.), Large Meteorite Impacts III: Geological Society of America Special Paper 384. Geological Society of America, Boulder, CO, pp. 85–115.

Kenkmann, T., Collins, G.S., Wünnemann, K., 2013. The modification stage of crater formation. In: Osinski, G.R., Pierazzo, E. (Eds.), Impact Cratering: Processes and Products. Blackwell Publishing, John Wiley & Sons, Hoboken, NJ, pp. 61–75.

Kerber, L., Head, J.W., Solomon, S.C., Murchie, S.L., Blewett, D.T., Wilson, L., 2009. Explosive volcanic eruptions on Mercury: eruption conditions, magma volatile content, and implications for interior volatile abundances. Earth Planet. Sci. Lett. 285 (3-4), 263–271. http://dx.doi.org/10.1016/j.epsl.2009.04.037.

Kerber, L., Head, J.W., Blewett, D.T., Solomon, S.C., Wilson, L., Murchie, S.L., Robinson, M.S., Denevi, B.W., Domingue, D.L., 2011. The global distribution of pyroclastic deposits on Mercury: the view from MESSENGER flybys 1–3. Planet. Space Sci. 59, 1895–1909. http://dx.doi.org/10.1016/j.pss.2011.03.020.

Kim, Y., Peacock, D.C.P., Sanderson, D.J., 2004. Fault damage zones. J. Struct. Geol. 26, 5035–5517. http://dx.doi.org/10.1016/j.jsg.2003.08.002.

Kinczyk, M.J., Prockter, L.M., Chapman, C.R., Susorney, H.C.M., 2016. A morphological evaluation of crater degradation on Mercury: revisiting crater classification using MESSENGER data. Lunar Planet. Sci. 47 abstract 1573, Houston, Texas.

King, G.C.P., Stein, R.S., Lin, J., 1994. Static stress changes and the triggering of earthquakes. Bull. Seismol. Soc. Am. 84, 935–953.

Le Feuvre, M., Wieczorek, M.A., 2011. Nonuniform cratering of the Moon and a revised crater chronology of the inner Solar System. Icarus 214, 1–20. http://dx.doi.org/10.1016/j.icarus.2011.03.010.

Melosh, H.J., 1984. Impact ejection, spallation, and the origin of meteorites. Icarus 59 (2), 234–260. http://dx.doi.org/10.1016/0019-1035(84)90026-5.

Morgan, J.V., Warner, M.R., Collins, G.S., Melosh, H.J., Christeson, G.L., 2000. Peak-ring formation in large impact craters: geophysical constraints from Chicxulub. Earth Planet. Sci. Lett. 183, 347–354. http://dx.doi.org/10.1016/S0012-821X(00)00307-1.

Morgan, J.V., Gulick, S.P., Bralower, T., Chenot, E., Christeson, G., Claeys, P., Cockell, C., Collins, G.S., Coolen, M.J., Ferrière, L., Gebhardt, C., Goto, K., Jones, H., Kring, D.A., Le Ber E., LofiJ., Long, X., Lowery, C., Mellett, C., Ocampo-Torres, R., Osinski, G.R., Perez-Cruz, L., Pickersgill, A., Poelchau, M., Rae, A., Rasmussen, C., Rebolledo-Vieyra, M., Riller, U., Sato, H., Schmitt, D.R., Smit, J., Tikoo, S., Tomioka, N., Urrutia-Fucugauchi, J., Whalen, M., Wittmann, A., Yamaguchi, K.E., Zylberman, W., 2016. The formation of peak rings in large impact craters. Science 354, 878–882. http://dx.doi.org/10.1126/science.aah6561.

Osinski, G.R, Spray, J.G., 2005. Tectonics of complex crater formation as revealed by the Haughton impact structure, Devon Island, Canadian High Arctic. Meteorit. Planet. Sci. 40, 1813–1834.

Peacock, D.C.P., Dimmen, V., Rotevatn, A., Sanderson, D.J., 2017. A broader classification of damage zones. J. Struct. Geol. 102, 179–192. http://dx.doi.org/10.1016/j.jsg.2017.08.004.

Rothery, D.A., Thomas, R.J., Kerber, L., 2014. Prolonged eruptive history of a compound volcano on Mercury: volcanic and tectonic implications. Earth Planet. Sci. Lett. 385, 59–67. http://dx.doi.org/10.1016/j.epsl.2013.10.023.

Schultz, R.A., Fossen, H., 2008. Terminology for structural discontinuities. Am. Assoc. Pet. Geol. Bull., vol. 92, 853–867. http://dx.doi.org/10.1306/02200807065.

Solomon, S.C., 1977. The relationship between crustal tectonics and internal evolution in the Moon and Mercury. Phys. Earth Planet. Inter. 15, 135–145. http://dx.doi.org/10.1016/0031-9201(77)90026-7.

Solomon, S.C., 1978. On volcanism and thermal tectonics on one-plate planets. Geophys. Res. Lett. 5 (6), 461–464. http://dx.doi.org/10.1029/GL005i006p00461.

Solomon, S.C., McNutt, R.L., Watters, T.R., Lawrence, D.J., Feldman, W.C., Head, J.W., Krimigis, S.M., Murchie, S.L., Phillips, R.J., Slavin, J.A., Zuber, M.T., 2008. Return to Mercury: a global perspective on MESSENGER's first Mercury flyby. Science 321 (5885), 59–62. http://dx.doi.org/10.1126/science.1159706.

Spray, J.G., 1997. Superfaults. Geology 25, 579–582. http://dx.doi.org/10.1130/0091-7613(1997)025<0579:S>2.3.CO;2.

Spudis, P.D., Guest, J.E., 1988. Stratigraphy and geologic history of Mercury. In: Vilas, F., Chapman, C.R., Matthews, M.S. (Eds.), Mercury. University of Arizona Press, Tucson, Ariz, pp. 118–164.

Thomas, R.J., Rothery, D.A., Conway, S.J., Anand, M., 2014. Long-lived explosive volcanism on Mercury. Geophys. Res. Lett. 41, 6084–6094. http://dx.doi.org/10.1002/2014GL061224.

Thomas, R.J., Rothery, D.A., Conway, S.J., Anand, M., 2015. Mechanisms of explosive volcanism on Mercury: implications from its global distribution and morphology. J. Geophys. Res. 119, 2239–2254. http://dx.doi.org/10.1002/2014JE004692.

Weider, S.Z., Nittler, L.R., Murchie, S.L., Peplowski, P.N., McCoy, T.J., Kerber, L., Klimczak, C., Ernst, C.M., Goudge, T.A., Starr, R.D., Izenberg, N.R., Klima, R.L., Solomon, S.C., 2016. Evidence from MESSENGER for sulfur-and carbon-driven explosive volcanism on Mercury. Geophys. Res. Lett. 43, 3653–3661. http://dx.doi.org/10.1002/2016GL068325.

Wieczorek, M.A., Neumann, G.A., Nimmo, F., Kiefer, W.S., Taylor, G.J., Melosh, H.J., Phillips, R.J., Solomon, S.C., Andrews-Hanna, J.C., Asmar, S.W., Konopliv, A.S., Lemoine, F.G., Smith, D.E., Watkins, M.M., Williams, J.G., Zuber, M.T., 2013. The crust of the Moon as seen by GRAIL. Science 339, 671–675. http://dx.doi.org/10.1126/science.1231530.

Wilson, L., Head, J.W., 2008. Volcanism on Mercury: a new model for the history of magma ascent and eruption. Geophys. Res. Lett. 35, L23205. http://dx.doi.org/10.1029/2008GL035620.

Xia, K., Ahrens, T.J., 2001. Impact induced damage beneath craters. Geophys. Res. Lett. 28, 3525–3527. http://dx.doi.org/10.1029/2001GL013001.